

Radiative neutron capture on a proton at BBN energies

S. Ando ^{a,b,1}, R. H. Cyburt ^{a,2}, S. W. Hong ^{b,3}, and C. H. Hyun ^{b,c,4},

^a*Theory Group, TRIUMF, 4004 Wesbrook Mall, Vancouver, B.C. V6T 2A3, Canada*

^b*Department of Physics and Institute of Basic Science, Sungkyunkwan University,
Suwon 440-746, Korea*

^c*School of Physics, Seoul National University, Seoul 151-742, Korea*

The total cross section for radiative neutron capture on a proton, $np \rightarrow d\gamma$, is evaluated at big bang nucleosynthesis (BBN) energies. The electromagnetic transition amplitudes are calculated up to next-to leading order within the framework of pionless effective field theory with dibaryon fields. We also calculate the $d\gamma \rightarrow np$ cross section and the photon analyzing power for the $d\vec{\gamma} \rightarrow np$ process from the amplitudes. The values of low energy constants that appear in the amplitudes are estimated by a Markov Chain Monte Carlo analysis using the relevant low energy experimental data. Our result agrees well with those of other theoretical calculations except for the $np \rightarrow d\gamma$ cross section at some energies estimated by an R-matrix analysis. We also study the uncertainties in our estimation of the $np \rightarrow d\gamma$ cross section at relevant BBN energies and find that the estimated cross section is reliable to within $\sim 1\%$ error.

PACS(s): 02.50.Ga, 02.70.Uu, 11.10.Ef, 25.40.Lw, 26.35.+c

¹E-mail:sando@meson.skku.ac.kr

²E-mail:cyburt@triumf.ca

³E-mail:swhong@skku.ac.kr

⁴E-mail:hch@meson.skku.ac.kr

1. Introduction

Primordial nucleosynthesis happens between 1 and 10^2 seconds after the big bang at temperatures ranging from $T \simeq 1$ MeV to 70 keV. (These are the temperatures of weak freeze out and the end of the D bottleneck, respectively). Predictions of primordial light element abundances, D, ^3He , ^4He and ^7Li , and their comparison with observations are a crucial test of the standard big bang cosmology. The uncertainties in these predictions are dominated by the nuclear physics input from reaction cross sections. Reaction databases are continuously updated [1, 2, 3], with more attention now paid to the error budget. In order to understand big bang nucleosynthesis (BBN) more clearly, it is essential to accurately measure these reaction cross sections at the energies relevant for BBN.

The radiative neutron capture on a proton, $np \rightarrow d\gamma$, is one of the key reactions for BBN, since this process is the starting point of the synthesis of the light elements (*i.e.* it determines the end of the D bottleneck). The cross sections of the $np \rightarrow d\gamma$ reaction have been measured by Suzuki *et al.* [4] and Nagai *et al.* [5]. Its inverse process, the photo-disintegration of the deuteron, $d\gamma \rightarrow np$, has had its cross section measured near threshold by Hara *et al.* [6] and Moreh *et al.* [7]⁵, and the photon analyzing power for the deuteron photo-disintegration are reported by Schreiber *et al.* [10] and Tornow *et al.* [11]. Although these data comprise an important data set, they nevertheless only sparsely sample the energies relevant for BBN. Hence an attempt at applying these experimental data directly to the BBN predictions would make the uncertainties larger.

Theoretical calculations suggest that theory errors can be sufficiently smaller than typical experimental uncertainties $\sim 5\%$, and that they can provide a very useful discriminant for theories and their perturbative schemes. BBN reaction compilations adopt these theory-based cross sections since they can provide more robust and accurate predictions than experiment alone. However, the uncertainties from the recent theoretical estimations of the cross section for $np \rightarrow d\gamma$ at BBN energies are considerably different from each other; 4% [12], 2 \sim 3% [13], and 1% [14]. These differences could lead to different uncertainties in the BBN predictions, and thus it is necessary to examine the relevant error budget for the $np \rightarrow d\gamma$ process with a new method.

Effective field theories (EFTs) provide a model-independent calculation and a systematic perturbation scheme in terms of Q/Λ in calculations of various low energy hadronic processes [15, 16], where Q is a typical momentum scale of a reaction in question and Λ is a large scale integrated out from effective Lagrangian. Since the energies relevant for BBN ($T \simeq 1$ MeV) are significantly smaller than the pion mass, we can consider the pions as heavy degrees of freedom and integrate them out of the Lagrangian. Pionless EFTs [17] have been intensively studied in various two-, three- and four-nucleon processes for the last decade (see, *e.g.*, Refs. [18, 19] for reviews and references therein). Convergence in the pionless EFT-based perturbative expansion turns out to be rather slow for the deuteron channel due to a relatively large expansion parameter, $Q/\Lambda \sim 1/3$ [20]. This large expansion parameter essentially determines the uncertainty estimates of the pionless EFT calculations. For example, in the next-to-next-to-next-to leading order (N^3LO)

⁵We do not include the data from Bishop *et al.* [8] in this work because of the wrong normalization factor of the data [9].

calculation of the $np \rightarrow d\gamma$ cross section at the BBN energies, Chen and Savage found a $(1/3)^3 \sim 4\%$ error [12]. Rupak pushed the calculation one order higher, *i.e.*, up to N⁴LO, and found a $(1/3)^4 \sim 1\%$ theoretical uncertainty in the cross section [14].

It has been suggested that the convergence of the pionless EFTs for the deuteron channel can be improved by adjusting the deuteron wave function so as to fit it to the asymptotic S -state normalization constant $Z_d = \gamma\rho_d/(1 - \gamma\rho_d)$ ($\gamma = \sqrt{m_N B}$ where B is the binding energy of the deuteron and ρ_d is its effective range) [21, 22, 23]. By introducing dibaryon fields which represent a resonance scattering state of the 1S_0 channel and the deuteron bound state of the 3S_1 channel, Beane and Savage showed that the dibaryon EFT (dEFT) without pions can naturally account for the long tail of the deuteron wave function in the renormalized dibaryon propagator at the deuteron pole [24].⁶ The slow convergence problem, however, was not fully resolved in dEFT. For instance, as discussed in detail in Ref. [28], when one includes the electromagnetic (EM) interaction into the np system in the framework of dEFT, vector(photon)-dibaryon-dibaryon (Vdd) vertices, which are classified in the subleading order in the previous work [24], give contributions comparable to those of the leading ones. In Ref. [28], we suggested a simple prescription to extract a LO contribution from the low energy constants (LECs) of the Vdd vertices (we will mention it below), and this re-ordering of the Vdd term has shown a satisfactory convergence rate similar to that reported in other EFT calculations. We employ this modified counting of the Vdd vertex, and confirm that this machinery is useful for the calculations of processes and observables considered here.

In this work, we calculate the cross sections of the $np \rightarrow d\gamma$ process at BBN energies, its inverse reaction $d\gamma \rightarrow np$, and the photon analyzing power for the $d\vec{\gamma} \rightarrow np$ process within the framework of dEFT up to next-to leading order (NLO). Values and uncertainties of LECs that appear in the amplitudes are estimated by a Markov Chain Monte Carlo (MCMC) analysis using the relevant low energy experimental data; the total cross section of the np scattering at the energies $\lesssim 5$ MeV, the rates of the $np \rightarrow d\gamma$ process, its inverse process $d\gamma \rightarrow np$, and the photon analyzing power in the $d\vec{\gamma} \rightarrow np$ process. Having fitted the values of the LECs, we compare our results with the experimental data mentioned above, and find that our statistical error bars of the $np \rightarrow d\gamma$ cross section are satisfactorily improved compared to the experimental ones. We also compare our result of the $np \rightarrow d\gamma$ cross section with other theoretical estimations, the pionless EFT calculation up to N⁴LO [14], a calculation with Argonne v18 (Av18) potential and the meson exchange current [29], and the result of an R-matrix analysis [30]. Our result agrees quite well with those of the previous EFT and Av18 potential model calculations within the uncertainties ($\sim 1\%$) estimated by MCMC. On the other hand we find significant ($\sim 4.6\%$) difference in the $np \rightarrow d\gamma$ cross sections from the R-matrix theory estimated at $E = 0.1$ and 1 MeV where E is the total two-nucleon kinetic energy in the center of mass frame. Since the various theoretical uncertainties from higher order corrections in the pionless EFT calculation have already been studied in Ref. [14] and the slow convergence

⁶Recently, dEFT has been employed in studying, *e.g.*, neutron-neutron fusion [25], muon capture on the deuteron [26], and the deeply-virtual Compton scattering dissociation of the deuteron and the EMC effect [27].

problem in the former pionless EFT calculations has been resolved in dEFT, we discuss that the theoretical estimations of the $np \rightarrow d\gamma$ cross section at the BBN energies are reliable with an uncertainty of $\lesssim 1\%$.

This paper is organized as follows. In Sect. 2, we present the pionless effective Lagrangian with dibaryon fields up to NLO. We calculate the amplitudes with the S - and P -wave np states and the cross sections for the $np \rightarrow d\gamma$ and $d\gamma \rightarrow np$ processes and the photon analyzing power for the $d\vec{\gamma} \rightarrow np$ process up to NLO in Sect. 3. Utilizing a Markov Chain algorithm, we determine the values and uncertainties of the LECs in Sect. 4. In Sect. 5, we compare the resulting observables to the experimental data and other theoretical estimations. In Sect. 6, we summarize our results and give discussion. In appendix A, we present the expressions of the renormalized dibaryon propagator and the S -wave NN scattering amplitudes, and show the relations between the LECs in the strong sector and the parameters in the effective range theory. In appendix B, we describe in detail the MCMC analysis in determining the LECs and cross sections.

2. Pionless effective Lagrangian with dibaryon fields

A pionless effective Lagrangian for nucleon and dibaryon fields interacting with an external vector field can be written as [24, 28]

$$\mathcal{L} = \mathcal{L}_N + \mathcal{L}_s + \mathcal{L}_t + \mathcal{L}_{st}, \quad (1)$$

where \mathcal{L}_N is the nucleon Lagrangian, \mathcal{L}_s and \mathcal{L}_t are the Lagrangian for the dibaryon fields in 1S_0 and 3S_1 channels, respectively. \mathcal{L}_{st} is the Lagrangian that accounts for the isovector EM interaction of the dibaryon fields.

\mathcal{L}_N in the heavy-baryon formalism reads

$$\mathcal{L}_N = N^\dagger \left\{ iv \cdot D + \frac{1}{2m_N} \left[(v \cdot D)^2 - D^2 - i[S^\mu, S^\nu] \left((1 + \kappa_V) f_{\mu\nu}^+ + (1 + \kappa_S) f_{\mu\nu}^S \right) \right] \right\} N, \quad (2)$$

where v^μ is the velocity vector satisfying $v^2 = 1$; we take $v^\mu = (1, \vec{0})$. S^μ is the spin operator $2S^\mu = (0, \vec{\sigma})$. $D_\mu = \partial_\mu - \frac{i}{2}\vec{\tau} \cdot \vec{\mathcal{V}}_\mu - \frac{i}{2}\mathcal{V}_\mu^S$, where $\vec{\mathcal{V}}_\mu$ and \mathcal{V}_μ^S are the external isovector and isoscalar vector currents, respectively. $f_{\mu\nu}^+ = \frac{\vec{\tau}}{2} \cdot (\partial_\mu \vec{\mathcal{V}}_\nu - \partial_\nu \vec{\mathcal{V}}_\mu)$ and $f_{\mu\nu}^S = \frac{1}{2}(\partial_\mu \mathcal{V}_\nu^S - \partial_\nu \mathcal{V}_\mu^S)$. m_N is the nucleon mass and κ_V (κ_S) is the isovector (isoscalar) anomalous magnetic moment of the nucleon, $\kappa_V = 3.706$ ($\kappa_S = -0.120$).

\mathcal{L}_s , \mathcal{L}_t , and \mathcal{L}_{st} for the dibaryon and two nucleon fields read

$$\mathcal{L}_s = \sigma_s s_a^\dagger \left[iv \cdot D + \frac{1}{4m_N} [(v \cdot D)^2 - D^2] + \Delta_s \right] s_a - y_s \left[s_a^\dagger (N^T P_a^{(^1S_0)} N) + \text{h.c.} \right], \quad (3)$$

$$\begin{aligned} \mathcal{L}_t &= \sigma_t t_i^\dagger \left[iv \cdot D + \frac{1}{4m_N} [(v \cdot D)^2 - D^2] + \Delta_t \right] t_i - y_t \left[t_i^\dagger (N^T P_i^{(^3S_1)} N) + \text{h.c.} \right] \\ &+ \left[\frac{1 + \kappa_S}{2m_N} - \frac{2l_2}{m_N \rho_d} \right] i \epsilon_{ijk} t_i^\dagger t_j B_k, \end{aligned} \quad (4)$$

$$\mathcal{L}_{st} = \left[-\frac{1 + \kappa_V}{2m_N} \left(\frac{r_0 + \rho_d}{2\sqrt{r_0 \rho_d}} \right) + \frac{l_1}{m_N \sqrt{r_0 \rho_d}} \right] (t_i^\dagger s_3 B_i + \text{h.c.}). \quad (5)$$

The covariant derivative for the dibaryon field is given by $D_\mu = \partial_\mu - iC\mathcal{V}_\mu^{ext}$, where \mathcal{V}_μ^{ext} is the external vector field and C is the charge operator of the dibaryon fields; $C = 0, 1, 2$ for nn , np , pp channels, respectively, and we have set $e = 1$. \vec{B} is the magnetic field given by $\vec{B} = \vec{\nabla} \times \vec{\mathcal{V}}^{ext}$. σ_t (σ_s) is the sign factor, Δ_t (Δ_s) is the difference between the dibaryon mass m_t (m_s) in the 3S_1 (1S_0) channel and the two-nucleon mass; $m_{t,s} = 2m_N + \Delta_{t,s}$, and $y_{s,t}$ are the dibaryon-nucleon-nucleon (dNN) coupling constants of the dibaryon spin singlet and triplet channels. In appendix A, these LECs in the strong sector are related to the parameters of the effective range theory. l_1 and l_2 are LECs of the Vdd vertices and can be fixed, for instance, by the thermal $np \rightarrow d\gamma$ rate and the deuteron magnetic moment, respectively. We note that we have separated the leading contributions from the coefficients in the Vdd vertices associated with l_1 and l_2 and fixed them mainly by one-body interactions, *i.e.*, the vector(photon)-nucleon-nucleon (VNN) couplings, as suggested in Ref. [28]. Consequently, l_1 and l_2 terms in this work give genuine NLO contributions. ρ_d and r_0 are the effective ranges for the deuteron and 1S_0 scattering state, respectively. $P_i^{(S)}$ is the projection operator for the $\mathcal{S} = {}^{2S+1}L_J$ channel. For the S and P waves which are dominant at low energies, the projection operators are given as [31];

$$\begin{aligned}
P_i^{(3S_1)} &= \frac{1}{\sqrt{8}}\sigma_2\sigma_i\tau_2, & P_a^{(1S_0)} &= \frac{1}{\sqrt{8}}\sigma_2\tau_2\tau_a, & P_a^{(1P_1)} &= \sqrt{\frac{3}{8}}\hat{p} \cdot \vec{\epsilon}\tau_a, \\
P_a^{(3P_0)} &= \frac{1}{\sqrt{8}}\sigma_2\vec{\sigma} \cdot \hat{p}\tau_2\tau_a, & P_a^{(3P_1)} &= \frac{\sqrt{3}}{4}\epsilon^{ijk}\epsilon^i\hat{p}^j\sigma_2\sigma^k\tau_2\tau_a, \\
P_a^{(3P_2)} &= \sqrt{\frac{3}{8}}\epsilon^{ij}\hat{p}^i\sigma_2\sigma^j\tau_2\tau_a, & \int \frac{d\Omega_{\hat{p}}}{4\pi}\text{Tr}(P_i^{(S)\dagger}P_j^{(S)}) &= \frac{1}{2}\delta_{ij},
\end{aligned} \tag{6}$$

where ϵ^i and ϵ^{ij} are $J=1$ and 2 polarization tensor, respectively, and σ_i (τ_a) with $i(a) = 1, 2, 3$ is the spin (isospin) operator.

We adopt the standard counting rules of dEFT [24]. Introducing an expansion scale $Q < \Lambda$ ($\simeq m_\pi$), we count magnitude of spatial part of the external and loop momenta, $|\vec{p}|$ and $|\vec{l}|$, as Q , and the time component of them, p^0 and l^0 , as Q^2 . Thus the nucleon and dibaryon propagators are of Q^{-2} and a loop gives a factor of Q^5 due to the 4-dimensional differential volume in the loop integration. The scattering lengths and effective ranges are counted as $Q \sim \{\gamma, 1/a_0, 1/\rho_d, 1/r_0\}$. This ensures, as discussed in the introduction, that one reproduces the long tail of the deuteron wavefunction characterized by $\sqrt{Z_d}$ and thus has good convergence [21, 22, 23]. Orders of vertices and diagrams are easily obtained by counting the numbers of these factors.

3. Amplitudes and cross sections

Diagrams for $np \rightarrow d\gamma$ up to NLO are depicted in Fig. 1. Diagrams (a) and (b) give only LO contributions. Diagram (c) consists of LO and NLO fractions and the NLO contributions from the diagram (c) stem from the LECs l_1 and l_2 , as discussed above.

Summing up the contributions of the diagrams (a), (b) and (c) in Fig. 1, we obtain the amplitudes for the initial 3S_1 and 1S_0 states as [24, 28]

$$i\mathcal{A}^{(a+b+c)}({}^3S_1) = -i(\vec{\epsilon}_{(d)}^* \times \vec{\epsilon}_i) \cdot (\vec{\epsilon}_{(\gamma)}^* \times \hat{k})$$

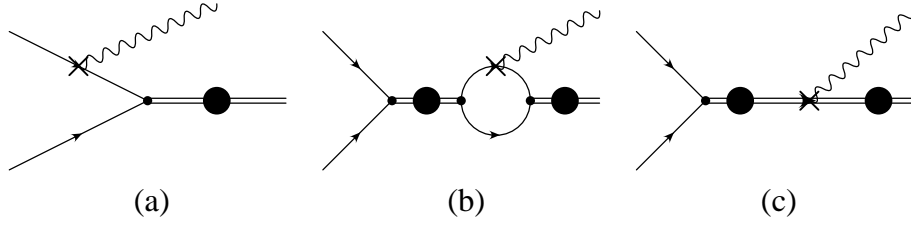


Figure 1: Diagrams contributing to $np \rightarrow d\gamma$ and $d\gamma \rightarrow np$: Diagrams (a) and (b) are of LO, $\mathcal{O}(Q^{1/2})$, while diagram (c) consists of LO and NLO terms, $\mathcal{O}(Q^{3/2})$. The single lines, the double lines with a filled circle (see Fig. 6 as well), and the wavy lines denote nucleons, renormalized dibaryons, and photons, respectively. VNN vertex “ \times ” in (a) and (b) and the LO part of Vdd vertex “ \times ” in (c) are proportional to $(1 + \kappa_S)$ and $(1 + \kappa_V)$ for the initial 3S_1 and 1S_0 channel, respectively. LECs l_1 and l_2 appear in the NLO part of the Vdd vertex “ \times ” in the diagram (c).

$$\times \sqrt{\frac{2\pi\gamma}{1 - \gamma\rho_d}} \frac{2}{m_N} \frac{1}{-\gamma - ip + \frac{1}{2}\rho_d(\gamma^2 + p^2)} \frac{\gamma^2 + p^2}{m_N} l_2, \quad (7)$$

$$i\mathcal{A}^{(a+b+c)}({}^1S_0) = \vec{\epsilon}_{(d)}^* \cdot (\hat{k} \times \vec{\epsilon}_{(\gamma)}^*) \sqrt{\frac{2\pi\gamma}{1 - \gamma\rho_d}} \frac{2}{m_N} \frac{1}{-\frac{1}{a_0} - ip + \frac{1}{2}r_0p^2} \\ \times \left\{ \frac{1 + \kappa_V}{2m_N} \left[\gamma - \frac{1}{a_0} - \frac{1}{4}(r_0 + \rho_d)\gamma^2 + \frac{1}{4}(r_0 - \rho_d)p^2 \right] + \frac{\gamma^2 + p^2}{2m_N} l_1 \right\}. \quad (8)$$

Here $2\vec{p}$ is the relative momentum of the two-nucleon system, and \vec{k} is the momentum of the outgoing photon; $p = |\vec{p}|$, $k = |\vec{k}|$, and $\hat{k} = \vec{k}/k$. $\vec{\epsilon}_{(d)}^*$ and $\vec{\epsilon}_{(\gamma)}^*$ are the polarization vectors for the outgoing deuteron and photon, respectively. a_0 is the scattering length in the 1S_0 channel. The LECs in the strong sector have been renormalized by the effective range parameters. See appendix A for details. We note that the isovector $M1$ amplitude (the 1S_0 channel), Eq. (8), has contributions from both LO and NLO. Whereas, the isoscalar $M1$ amplitude (the 3S_1 channel), Eq. (7), has no LO contribution due to the orthogonality between the bound and scattering states for the 3S_1 channel, but non-zero amplitude proportional to l_2 appears at NLO.

From the diagram (a) in Fig. 1, amplitudes with initial P -waves are obtained as;

$$i\mathcal{A}^{(a)}({}^3P_0) = -i\vec{\epsilon}_{(\gamma)}^* \cdot \vec{\epsilon}_{(d)}^* \sqrt{\frac{2\pi\gamma}{1 - \gamma\rho_d}} \frac{2}{3m_N} \frac{p}{(\gamma^2 + p^2)}, \quad (9)$$

$$i\mathcal{A}^{(a)}({}^3P_1) = -i\vec{\epsilon}_1 \cdot (\vec{\epsilon}_{(\gamma)}^* \times \vec{\epsilon}_{(d)}^*) \sqrt{\frac{2\pi\gamma}{1 - \gamma\rho_d}} \sqrt{\frac{2}{3}} \frac{p}{m_N(\gamma^2 + p^2)}, \quad (10)$$

$$i\mathcal{A}^{(a)}({}^3P_2) = \epsilon_2^{ij} \epsilon_{(\gamma)}^{*i} \epsilon_{(d)}^{*j} \sqrt{\frac{2\pi\gamma}{1 - \gamma\rho_d}} \frac{2}{\sqrt{3}m_N} \frac{p}{(\gamma^2 + p^2)}. \quad (11)$$

We note that the diagrams (b) and (c) in Fig. 1 do not contribute to the P -wave amplitudes

because the states of the renormalized dibaryon propagator are only the S -waves.

Having the amplitudes calculated above, we can easily obtain the expressions of the cross sections of the $np \rightarrow d\gamma$ and $d\gamma \rightarrow np$ processes and the analyzing power for the $d\vec{\gamma} \rightarrow np$ process. The total cross section of the $np \rightarrow d\gamma$ process in the CM frame reads [24, 28]

$$\sigma = \frac{\alpha(\gamma^2 + p^2)}{4p} \sum_{\text{spin}} |\mathcal{A}|^2, \quad (12)$$

where α is the fine structure constant.⁷

The total cross section of the photo-disintegration of the deuteron, $d\gamma \rightarrow np$, has a simple relation with the cross section of its inverse process as [12]

$$\sigma(\gamma d \rightarrow np) = \frac{2m_N(E_\gamma - B)}{3E_\gamma^2} \sigma(np \rightarrow d\gamma), \quad (13)$$

where E_γ is the photon energy. Since we have already obtained the np -capture cross section, the calculation of $\sigma(\gamma d \rightarrow np)$ is straightforward.

The photon analyzing power $\Sigma(\theta)$ with the linearly polarized photons in the $d\vec{\gamma} \rightarrow np$ process is defined as $\Sigma(\theta) \equiv (N_\parallel - N_\perp)/(N_\parallel + N_\perp)$ where N_\parallel and N_\perp are the number of outgoing neutrons counted in and out of the horizontal γ -ray polarization plane, respectively, and θ is the angle between the incoming photon and outgoing neutron in the laboratory frame. This quantity is related to the $M1$ and $E1$ contributions to the total cross sections of the $d\gamma \rightarrow np$ process, σ_{M1} and σ_{E1} , respectively. The relation can be found *e.g.*, in Eq. (4) of Ref. [10], which reads

$$\Sigma(\theta) = \frac{\frac{3}{2}\sigma_{E1}\sin^2\theta}{\sigma_{M1} + \frac{3}{2}\sigma_{E1}\sin^2\theta}. \quad (14)$$

σ_{M1} and σ_{E1} are easily calculated by using Eqs. (12, 13) and the expressions of the $M1$ and $E1$ amplitudes obtained in Eqs. (7, 8, 9, 10, 11).

4. Parameter determination from experimental data

In this section, we determine the values and uncertainties of the LECs that appear in our results from the relevant low energy experimental data. The cross sections and photon analyzing power obtained from the amplitudes in Eqs. (7, 8, 9, 10, 11) depend on six parameters; a_0 , r_0 , γ , ρ_d , l_1 , and l_2 . γ and l_2 are precisely determined by the deuteron binding energy B and magnetic moment μ_d , respectively. Using the relation, $\mu_d = 1 + \kappa_S + Z_d l_2$, we have $l_2 = -0.0154$ fm. It is ~ 50 times smaller than the value of

⁷In obtaining the total cross section, the following identities are useful.

$$\sum_{\text{spin}} |i\vec{\epsilon}_{(d)}^* \cdot (\hat{k} \times \vec{\epsilon}_{(\gamma)}^*)|^2 = 2, \quad \sum_{\text{spin}} |\vec{\epsilon}_{(\gamma)}^* \cdot \vec{\epsilon}_{(d)}^*|^2 = 2, \quad \sum_{\text{spin}} |\vec{\epsilon}_1 \cdot (\vec{\epsilon}_{(\gamma)}^* \times \vec{\epsilon}_{(d)}^*)|^2 = 4, \quad \sum_{\text{spin}} |\epsilon_2^{ij} \epsilon_{(\gamma)}^{*i} \epsilon_{(d)}^{*j}|^2 = \frac{10}{3}.$$

We ignore the amplitude for the 3S_1 channel in Eq. (7), as will be discussed later.

l_1 in Table 1 (and the expressions for the l_1 and l_2 terms in the amplitudes are almost identical). We will consider the error of the cross section at the order of 0.1%, so we neglect the amplitude in Eq. (7) from the 3S_1 channel in the following calculations. Thus, the parameters a_0 , r_0 , ρ_d , and l_1 are determined from the low energy experimental data, whereas γ is fixed from B and treated as a constraint in the fitting.

We fit these parameters to the low energy np data with a Markov Chain Monte Carlo (MCMC) analysis using the Metropolis algorithm [32]. This method is more efficient in exploring parameter space than creating a multi-dimensional grid of parameter values and interpolating to find the underlying likelihood distribution and favored parameter values. The method is a random walk constrained to “walk” in regions of low χ^2 . As the χ^2 increases for a particular step, the probability of the step being accepted into the chain decreases. This “walk” explores the allowed parameter space, and if long enough will explore all channels of parameter degeneracy. The resulting sample, then provides a direct probe of the parameter likelihood, and can be used to determine, *e.g.*, the means, standard deviations and correlations of the parameters. It also provides an accurate way of propagating the uncertainties and correlations of the parameters into the cross section uncertainties, which depend non-linearly on the parameters. One drawback is that this method is not particularly efficient at sampling multi-peaked distributions. The random walk can become trapped in a local minimum. For the case we are considering, the 5-dimensional likelihood distribution is singly peaked (*i.e.* a unique solution exists).

We now list the low energy experimental data employed in our fitting. To include the high precision measurements of the deuteron binding energy, we adopt the value of $B = 2.2245671 \pm 0.0000042$ MeV⁸ [34] as the additional constraint mentioned above. This accurate value of B gives the uncertainty of γ in the order of 10^{-6} , thus it is effectively fixed, independent from the other constraints. The np -scattering data are found on the NN-Online website [35]. We restrict ourselves to the angle-integrated scattering cross sections with center-of-mass energies $\lesssim 5$ MeV, and have $N_{sct} = 2124$ data points. We adopt the 2 thermal neutron capture cross sections from Cox *et al.* [36] (334.2 ± 0.5 mb) and Cokinos and Melkonian [37] (332.6 ± 0.7 mb),⁹ and also adopt the np -capture data of Suzuki *et al.* [4] and Nagai *et al.* [5], the photo-dissociation cross section data by Hara *et al.* [6] and Moreh *et al.* [7], and the photon analyzing power data from Schreiber *et al.* [10] and Tornow *et al.* [11].

Using the experimental data mentioned above, we fit these parameters employing the MCMC analysis. The steps in doing the MCMC analysis are described in detail in appendix B. We initialize the Markov chain at the point in 5 dimensional parameter space that minimizes the χ^2 . After verifying that the χ^2 had only one minimum, we did not

⁸The quoted deuteron binding energy is a weighted average of the available measurements. The error is the weighted dispersion about the mean, recommended by [3, 33] because standard techniques underestimate uncertainties when data are discrepant.

⁹In a private communication mentioned in [38], the Cox *et al.*’s thermal cross section is renormalized from 334.2 to 333.9 mb. This likely indicates hidden systematics in the experiment and subsequently larger (and unacknowledged) uncertainties, though we adopt the original published number. In addition, the thermal np capture rate, $\sigma = (334 \pm 3)$ mb, has been estimated by T.-S. Park *et al.* in the calculation of pionful effective field theory [39].

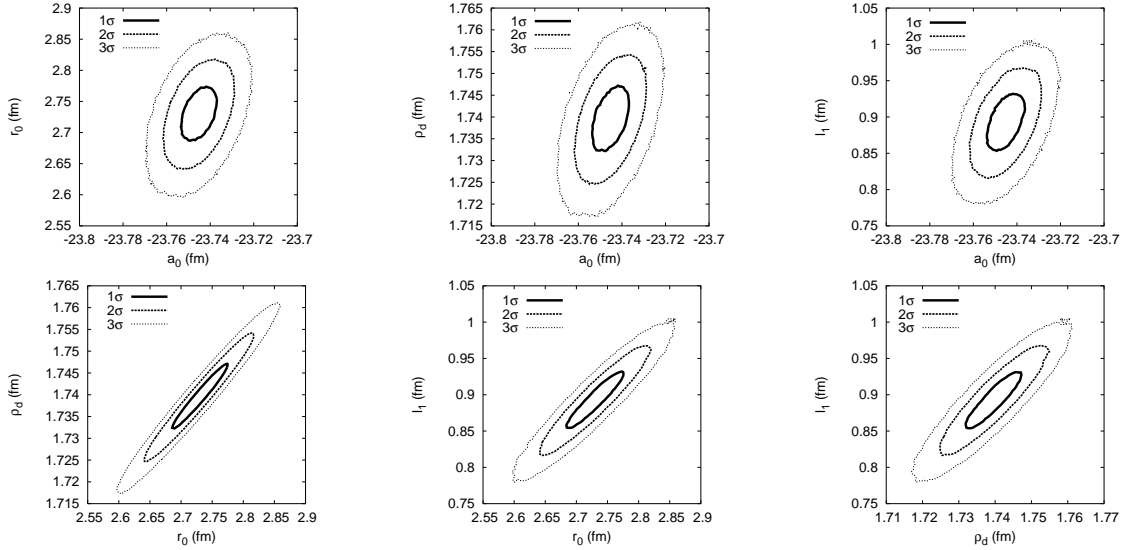


Figure 2: Contour plots of two dimensional parameter spaces for 5 dimensional probability distribution generated by the MCMC analysis. We draw the contours of 1,2, and 3 σ for each set of the parameters, a_0 , r_0 , ρ_d , and l_1 , whereas B is effectively fixed at the observed value and uncorrelated with the other parameters, and thus not shown.

need to run more than one Markov chain, making the analysis much more efficient. We display, in Fig. 2, two dimensional contour plots of 1, 2, and 3 σ for each set of parameters, a_0 , r_0 , ρ_d , l_1 from our 5 dimensional probability distribution generated from the MCMC analysis. We note that since B is effectively fixed and uncorrelated with the other parameters, contour plots with B are not necessary. “MCMC” in Table 1 are the average parameter values and standard deviations from this analysis with the total number of the data $N_{\text{tot}} = 2147$ and the minimum χ^2 , $\chi_{\text{tot,min}}^2 = 2303.00$. (For more details, see Table 4 in the appendix B.) These parameter values agree well with prior determinations shown in “Prev. Meth.” in the same table. The small ($\lesssim 2\%$) differences between “MCMC” and “Prev. Meth.” could be interpreted as effects from either higher order corrections not included in our calculation or simply statistical fluctuations. Also in Table 1, we show the correlations of the parameters. We find weak correlations of a_0 with the three parameters r_0 , ρ_d , and l_1 and strong correlations among these three parameters. Though we formally counted the four parameters as in the same order in this work, this may indicate the existence of a perturbative series that the contribution of a_0 is the LO one and the three parameters are in the same order (NLO), as already discussed in Ref. [20].

5. Numerical results

First, we present our numerical results obtained by using the fitted values of the parameters “MCMC” in Table 1, and compare them with the experimental data relevant to the BBN energies. We plot in Fig. 3 the total cross section (in mb) of $np \rightarrow d\gamma$ multiplied by the speed (in m/ns) of the neutron in the laboratory frame as a function of the incident energy of the neutron E_n . We also plot the $M1$ and $E1$ contributions to the total

	Prev. Meth.	MCMC	Correlations			
			a_0	r_0	ρ_d	l_1
a_0	-23.749 ± 0.008	-23.745 ± 0.008	1.000	0.433	0.464	0.496
r_0	2.81 ± 0.05	2.730 ± 0.044	0.433	1.000	0.975	0.936
ρ_d	1.760 ± 0.005	1.740 ± 0.007	0.464	0.975	1.000	0.898
l_1	0.782 ± 0.022	0.893 ± 0.038	0.496	0.935	0.898	1.000

Table 1: Values and correlations of the parameters. The values of the parameters obtained are in units of fm. “Prev. Meth.” are the adopted parameter values from previous works; of these a_0 , r_0 , and ρ_d are from Ref. [40] and l_1 from the thermal np capture rates [28]. “MCMC” is obtained by the MCMC analysis (χ^2 -fit) by using the low energy experimental data. Also shown are the parameter correlations. They are defined by $COR(i, j) = COV(i, j) / (\sigma_{\text{stat.}}(i)\sigma_{\text{stat.}}(j))$, where $COV(i, j)$ is the covariance between the i^{th} and j^{th} parameters and $\sigma_{\text{stat.}}(i)$ is the statistical uncertainty of the i^{th} parameter.

capture cross section in Fig. 3, where the $M1$ contribution comes from the amplitude of the initial 1S_0 state in Eq. (8) and the $E1$ contribution from the amplitudes of the initial P -wave states in Eqs. (9,10,11). At very small energies, the $M1$ contribution overwhelms the $E1$ one. They become similar at around $E_n \sim 0.45$ MeV and after that, the cross section is dominated by the $E1$ contribution.¹⁰ The experimental data of $np \rightarrow d\gamma$ are compared with our result in Fig. 3. Our results lie within the errors (5~6 %) of all the data by Suzuki *et al.* and Nagai *et al.*. In Fig. 4, we plot our result of the cross section of the $d\gamma \rightarrow np$ process and also separate the contributions from the $M1$ and $E1$ transition amplitudes. Recent measurement of the cross section at the BBN energies is reported by Hara *et al.* [6]. An old datum by Moreh *et al.* [7] is also included in the figure. Our result agrees well with these experimental data within the error bars.¹¹ In Fig. 5, we plot our results of $\Sigma(\theta)$ at $\theta = 90^\circ$ and 150° where experimental data are available [10, 11]. We find good agreement between our predictions and the experimental data. The error bars estimated for these quantities, discussed in detail below, are much improved compared to those of the experimental data.

Now, we compare our results with the predictions of the $np \rightarrow d\gamma$ cross sections at the BBN energies from various theories in Table 2. Our results, “MCMC” and “Prev. Meth.”, in Table 2 are calculated from the amplitudes in dEFT up to NLO by a MCMC analysis and by using the values of the “Prev. Meth.” parameters in Table 1, respectively.

¹⁰The contributions of $M1$ and $E1$ transitions to the total cross section of $np \rightarrow d\gamma$ and $d\gamma \rightarrow np$ are not disentangled in the measurements, but the role of each amplitude can be studied from the measurement of $\Sigma(\theta)$.

¹¹One may notice a departure (more than 1%) of our estimation from *the center values* of experimental data in Figs. 3 and 4. This is because the curves plotted in the figures are mainly determined by the other data: *e.g.*, the np scattering data have a prime role to determine the energy dependence of the curves, whereas the accurate thermal np capture rates determine the normalization of them. However, as verified by the good χ^2 , the curves are well within the experimental error bars.

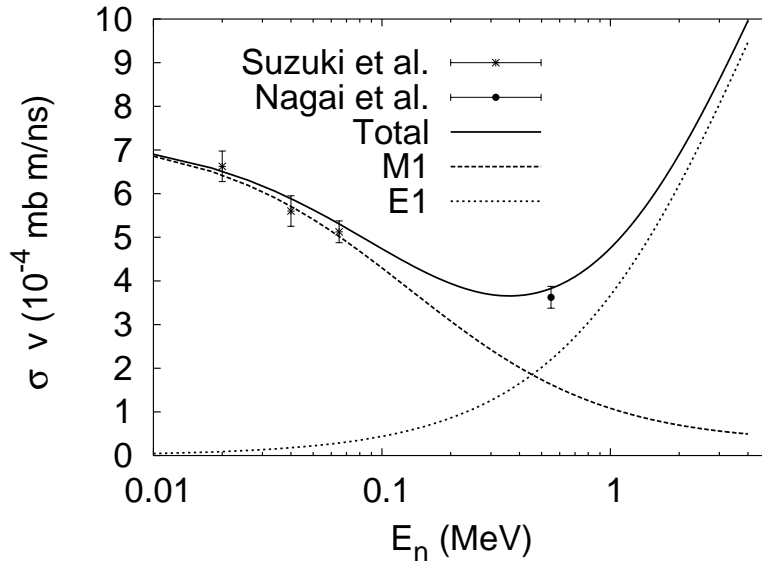


Figure 3: Total cross section of $n + p \rightarrow d + \gamma$ in units of mb multiplied by neutron speed in m/ns. Neutron energy E_n is in the laboratory frame. Dashed and dotted curves are the $M1$ and $E1$ contributions to the total cross section, respectively. The experimental data are from Suzuki *et al.* [4] and Nagai *et al.* [5].

E (MeV)	Cross section (mb)				
	MCMC	Prev. Meth.	Rupak[14]	Nakamura[29]	Hale[30]
1.265×10^{-8}	333.8(15)	333.7(15)	334.2(0)	335.0	332.6(7)
5×10^{-4}	1.667(8)	1.666(8)	1.668(0)	1.674	1.661(7)
1×10^{-3}	1.171(5)	1.171(5)	1.172(0)	1.176	1.167(2)
5×10^{-3}	0.4979(23)	0.4976(21)	0.4982(0)	0.4999	0.4953(11)
1×10^{-2}	0.3322(15)	0.3319(14)	0.3324(0)	0.3335	0.3298(9)
5×10^{-2}	0.1079(5)	0.1079(4)	0.1081(0)	0.1084	0.1052(9)
0.100	0.0634(3)	0.0634(2)	0.06352(5)	0.06366	0.0605(10)
0.500	0.0341(2)	0.0343(1)	0.0341(2)	0.03416	0.0338(8)
1.00	0.0349(3)	0.0352(1)	0.0349(3)	0.03495	0.0365(8)

Table 2: Theoretical predictions of the total cross section of the $n + p \rightarrow d + \gamma$ process at the BBN energies. E is the energy of two nucleons in the center of mass frame. See the text for details.

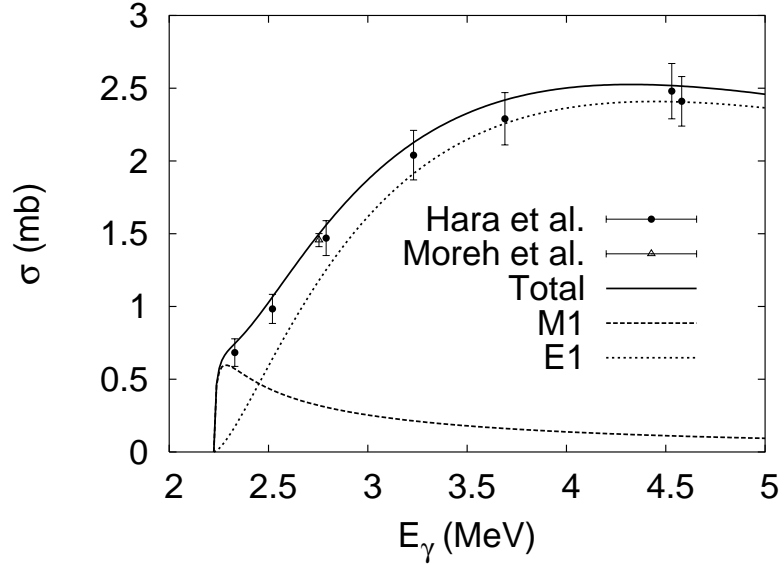


Figure 4: Total cross section for the $d + \gamma \rightarrow n + p$ process. Dashed and dotted curves represent the $M1$ and $E1$ contributions to the total cross section, respectively. The experimental data are from Hara *et al.* [6] and Moreh *et al.* [7].

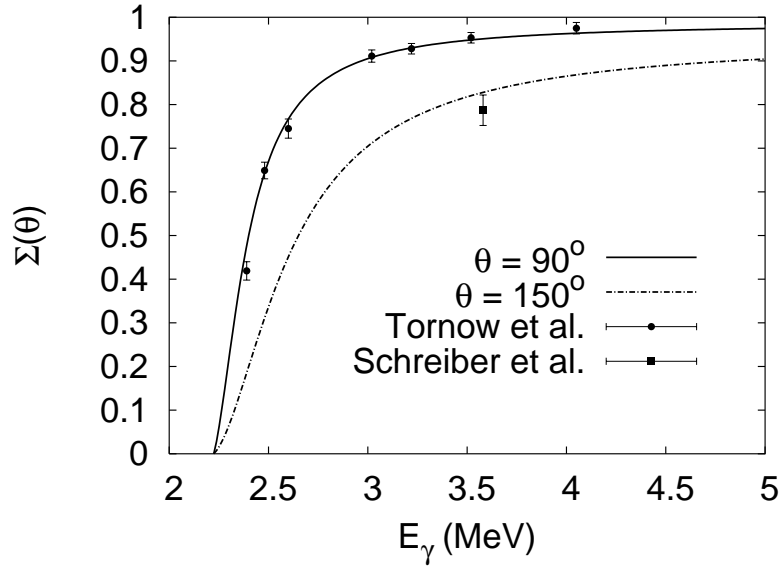


Figure 5: Photon analyzing power $\Sigma(\theta)$ for the $d + \gamma \rightarrow n + p$ process. We plot our results at $\theta = 90^\circ$ and 150° . The experimental data are from Schreiber *et al.* ($\theta = 150^\circ$) [10] and Tornow *et al.* ($\theta = 90^\circ$) [11].

We note that the values of the cross section in the column “MCMC” are the most likely cross section values with 68.3% central confidence limits. Thus we find that the error bars for the cross section are $\lesssim 1\%$ ¹². Values obtained by Rupak [14] in Table 2 are from the pionless EFT (without dibaryon fields) up to N⁴LO and those by Nakamura [29] are from the potential model calculation using wave functions from the Argonne v18 potential and meson exchange currents. The results by Hale are obtained from an R-matrix analysis [30]. There is good agreement between our two results, “MCMC” and “Prev. Meth.”, up to 0.1 MeV, whereas they show small differences ($\sim 0.6\%$ and 0.9%) at $E = 0.5$ and 1 MeV. We also find good agreement between the “MCMC” analysis with that of the pionless EFT up to N⁴LO by Rupak ($\lesssim 0.2\%$) and with that of the accurate potential model including the exchange current by Nakamura ($\lesssim 0.5\%$), while the results of the R-matrix theory at $E = 0.1$ and 1 MeV significantly differ from the other estimations by $\sim 4.6\%$.

Finally, we determine and present a thermal capture rate and relative error taking the recommended cross section from “MCMC” in Table 2 for use in BBN computer codes:

$$\begin{aligned}
f &= N_A \langle \sigma v \rangle = 44216.0 [\text{cm}^3 \text{ s}^{-1} \text{ g}^{-1}] (1 + 3.75191 T_9 + 1.92934 T_9^2 \\
&\quad + 0.746503 T_9^3 + 0.0197023 T_9^4 + 3.00491 \times 10^{-6} T_9^5) \\
&\quad / (1 + 5.4678 T_9 + 5.62395 T_9^2 + 0.489312 T_9^3 + 0.00747806 T_9^4), \quad (15) \\
\delta f / f &= 0.00449213 (1 + 3.08947 T_9 + 0.13277 T_9^2 + 1.66472 T_9^3) \\
&\quad / (1 + 2.75245 T_9 + 1.40958 T_9^2 + 0.8791 T_9^3), \quad (16)
\end{aligned}$$

where T_9 is a dimensionless temperature defined by $T_9 = T/(10^9 K)$. Using the thermal rates for the np -capture reaction from “MCMC dEFT”, Rupak, and Hale, we show in Table 3 how the light element abundance predictions vary with the different np -capture cross sections. We find little change for the mass fraction of ⁴He, Y_p and the mole fractions ³He/H, a tiny ($\sim 0.6\%$) change for D/H, and a small ($\sim 2.9\%$) change for ⁷Li/H in the predicted light element abundances. Differences between the light element predictions are not significant compared to the current estimated errors in the BBN predictions. In fact, the error budget in the BBN predictions is dominated by the errors in other reactions such as $d(p, \gamma)^3\text{He}$ and $^3\text{He}(\alpha, \gamma)^7\text{Be}$ (see, *e.g.*, Ref. [3] for more details). We have verified that the np -capture rate is not yet a major source of uncertainty in the light element abundance predictions.

6. Conclusions and discussion

In this work, we calculated the total cross sections for the $np \rightarrow d\gamma$ and $d\gamma \rightarrow np$ processes and the photon analyzing power in the $d\vec{\gamma} \rightarrow np$ process at the energies relevant to BBN. The pionless EFT that incorporates dibaryon fields was employed, and the transition amplitudes were calculated up to NLO. The values of the parameters (equivalently the LECs in effective Lagrangian) and their uncertainties are evaluated by a MCMC analysis (χ^2 -fit) using the relevant low energy experimental data. Comparing our results with the experimental data and the previous theoretical estimations, we find good agreement

¹²One should note that the error bars of the 68.3% confidence limits are different from (and larger than) those of the standard deviation in multi-dimensional fits, whose typical error bars are $\lesssim 0.3\%$ [41].

np -capture rate	Y_p	D/H $\times 10^5$	${}^3\text{He}/\text{H} \times 10^6$	${}^7\text{Li}/\text{H} \times 10^{10}$
MCMC dEFT	0.24852	2.5467	10.0921	4.4646
Rupak [14]	0.24853	2.5434	10.0920	4.4902
Hale [13]	0.24849	2.5580	10.0864	4.3632

Table 3: The table shows how the light element abundance predictions vary with different np -capture cross sections. The nuclear rate compilation from [3] was adopted, varying only the np -capture rate. In fact, these predictions follow the simple abundance scalings (Eqs. (44-47) in Ref. [3]), using relative values of the np -capture cross sections at the end of the D bottleneck ($E \sim 0.07$ MeV).

within the estimated uncertainties ($\lesssim 1\%$) except for the np -capture rate estimated by the R-matrix analysis at $E = 0.1$ and 1 MeV where E is the initial energy for two-nucleon in the CM frame. These two values estimated by the R-matrix theory are considerably different from the other theoretical estimations by $\sim 4.6\%$. Therefore, it would be important to experimentally measure the np -capture cross sections at these energies to resolve this significant discrepancy.

Now we are in the position to discuss the uncertainties of $np \rightarrow d\gamma$ cross section at BBN energies. As discussed earlier, the EFT calculations provide model-independent expression for the amplitudes with a systematic perturbative scheme. In the pionless EFT calculation up to N⁴LO by Rupak, various corrections in the higher order terms have been taken into account and it has been concluded that the *theoretical* uncertainty up to the N⁴LO calculation in the $np \rightarrow d\gamma$ cross section is less than 1%. The effective range corrections are resummed in dEFT, and so the convergence of dEFT is better than the pionless EFTs. Thus we expect that the contributions from the higher terms, *i.e.*, the theoretical uncertainties in our calculation, to be less than Rupak’s estimation. With the overall good agreement between our MCMC analysis and the Rupak and Nakamura calculations, the conclusion that the theoretical uncertainties in the $np \rightarrow d\gamma$ cross sections is $\lesssim 1\%$ is well justified. The disagreement with the R-matrix analysis could be inferred from problems that R-matrix theory has in describing non-resonant reactions.

Most of the recent theoretical calculations, as seen in Table 2, predict similar results with similar uncertainties, and the accuracy of the calculations is better than the np -capture experimental results at present. This is the case mainly because there are a lot of accurate experimental data for the np scattering and, we could accurately constrain the four effective range parameters from them. We had only one additional LEC l_1 to fit from the low energy $np \rightarrow d\gamma$ and $d\gamma \rightarrow np$ cross sections and the photon analyzing power for the $d\vec{\gamma} \rightarrow np$ process. This situation, however, will change once we start studying other processes involving more than two nucleons for BBN, facing significant model dependence and lack of experimental data. As discussed in Ref. [42], the EFT approaches would be useful in studying few-body nuclear astrophysical processes because it provides simple model-independent expressions of the amplitudes with a finite number of LECs as well

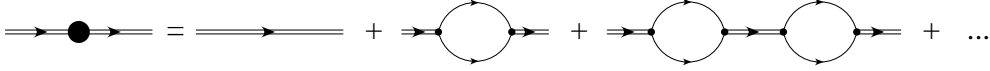


Figure 6: Diagrams for “dressed” dibaryon propagator at leading order. A double (single) line stands for a dibaryon (nucleon) field.

as a systematic expansion scheme.¹³ We expect that the combination of dEFT and the MCMC analysis can be a useful tool to estimate reliable uncertainties of few-body nuclear reactions for BBN with the aid of relevant low energy experimental data.

Acknowledgments

We are thankful to S. X. Nakamura and G. M. Hale for providing us with their numerical results. SA thanks J.-W. Chen, H. W. Hammer, L. Platter, Y. Nagai, A. Hosaka, K. Kubodera, D.-P. Min, M. Rho, and T. Kajino for discussions and communications. SA also thanks the Institute for Nuclear Theory at the University of Washington for its hospitality and partial support during the completion of this work. SWH thanks B. K. Jennings and TRIUMF for hospitality during his sabbatical leave. SA is supported by Korean Research Foundation and The Korean Federation of Science and Technology Societies Grant funded by Korean Government (MOEHRD, Basic Research Promotion Fund). This work is supported in part by the Natural Sciences and Engineering Research Council of Canada and by Faculty Research Fund, Sungkyunkwan University, 2004.

Appendix A

In this appendix we review the derivation of the renormalized dibaryon propagator from the low energy S -wave NN scattering [24, 28].

The LEC’s $\sigma_{s,t}$ and $y_{s,t}$ in the effective Lagrangian, Eqs. (3) and (4), can be fixed from the effective range parameters of the np scattering in 1S_0 and 3S_1 states. Firstly, we derive “dressed” dibaryon propagators. LO diagrams for the dressed dibaryon propagators in the S wave channels are depicted in Fig. 6. Since the insertion of the two-nucleon one-loop diagram does not alter the order of the diagram, the two-nucleon bubbles in the propagators should be summed up to infinite order. Thus the inverse dressed dibaryon propagators for the spin singlet (s) (1S_0) and triplet (t) (3S_1) channels in the center-of-mass (CM) frame read

$$\begin{aligned}
 iD_{s,t}^{-1}(p) &= i\sigma_{s,t}(E + \Delta_{s,t}) + iy_{s,t}^2 \frac{m_N}{4\pi}(ip) \\
 &= i\frac{m_N y_{s,t}^2}{4\pi} \left[\frac{4\pi\sigma_{s,t}\Delta_{s,t}}{m_N y_{s,t}^2} + \frac{4\pi\sigma_{s,t}E}{m_N y_{s,t}} + ip \right], \quad (17)
 \end{aligned}$$

where we have calculated the two-nucleon one-loop diagram using the dimensional regularization. p is the magnitude of the nucleon momentum in the CM frame, and E is the total energy $E \simeq p^2/m_N$.

¹³Recently, the $nd \rightarrow ^3\text{H}\gamma$ process has been studied in the pionless dEFT [43].

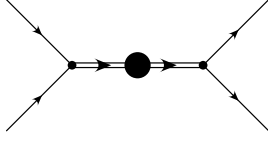


Figure 7: Diagram for the NN scattering amplitudes. The dNN vertex is proportional to $y_{s,t}$ and the propagator of the dressed dibaryon field (a double line with a filled circle) is obtained from the diagram in Fig. 6.

The S -wave NN scattering amplitudes for both spin channels obtained from Fig. 7 read

$$i\mathcal{A}_{s,t} = (-iy_{s,t})(iD_{s,t}(p))(-iy_{s,t}) = \frac{4\pi}{m_N} \frac{i}{-\frac{4\pi\sigma_{s,t}\Delta_{s,t}}{m_N y_{s,t}^2} - \frac{4\pi\sigma_{s,t}}{m_N^2 y_{s,t}^2} p^2 - ip}, \quad (18)$$

and they are related to the S -matrix via

$$S_{s,t} - 1 = e^{2i\delta_{s,t}} - 1 = \frac{2ip}{p \cot\delta_{s,t} - ip} = i \left(\frac{p m_N}{2\pi} \right) \mathcal{A}_{s,t}, \quad (19)$$

where $\delta_{s,t}$ are the S -wave phase shifts. The effective range expansion reads

$$p \cot\delta_s = -\frac{1}{a_0} + \frac{1}{2}r_0 p^2 + \dots, \quad p \cot\delta_t = -\gamma + \frac{1}{2}\rho_d(p^2 + \gamma^2) + \dots, \quad (20)$$

for the 1S_0 and 3S_1 channel, respectively. Comparing the expressions of the amplitudes in Eqs. (18) and (19), one has $\sigma_{s,t} = -1$ and

$$y_s = \frac{2}{m_N} \sqrt{\frac{2\pi}{r_0}}, \quad D_s(p) = \frac{m_N r_0}{2} \frac{1}{\frac{1}{a_0} + ip - \frac{1}{2}r_0 p^2}, \quad (21)$$

$$y_t = \frac{2}{m_N} \sqrt{\frac{2\pi}{\rho_d}}, \quad D_s(p) = \frac{m_N \rho_d}{2} \frac{1}{\gamma + ip - \frac{1}{2}\rho_d(p^2 + \gamma^2)} = \frac{Z_d}{E + B} + \dots, \quad (22)$$

where Z_d is the wavefunction normalization factor of the deuteron around deuteron binding energy B . Ellipsis denotes corrections that are finite or vanish at $E = -B$. Thus one has

$$Z_d = \frac{\gamma \rho_d}{1 - \gamma \rho_d}, \quad (23)$$

which is the same as the asymptotic S -wave normalization constant.

Appendix B: Running a MCMC

In this appendix we describe the steps in doing the MCMC analysis for determining the $D = 5$ parameters and cross sections.

1. Localizing the chain by minimizing the χ^2 .

The evolution of a Markov chain is governed by the χ^2 values at various points in parameter space. We adopt the standard definition:

$$\chi^2 = \sum_i \left(\frac{\sigma_i(\text{thry}) - \sigma_i(\text{expt})}{\delta\sigma_i(\text{expt})} \right)^2, \quad (24)$$

where $\sigma_i(\text{expt})$ and $\delta\sigma_i(\text{expt})$ are the experimentally measured values (*e.g.* cross sections) and their total errors, respectively, and $\sigma_i(\text{thry})$ is the evaluated theoretical value; the sum is over all data points.

Before we evaluate the χ^2 , we should pick some reasonable model space. Generally relying on previous works or positive definiteness, one can place limits on the allowed parameter space. Of course one can expand this model space if a minimum is found at an edge of the parameter space.

We begin by selecting an initial set of parameters (\vec{p}_0) and estimate step sizes ($\delta\vec{p}_0$) to be some fraction of the size of each parameter space direction. Drawing a set of random numbers \vec{z} with zero mean and unit variance (*e.g.* a Gaussian-normal random number), one can determine a new set of parameters via the relation:

$$p = p_0 + \delta p_0 z. \quad (25)$$

Evaluating the $\chi^2(\vec{p})$ of this new set of parameters, and comparing to the original $\chi^2(\vec{p}_0)$ we can determine if the new parameter values better describe the data. If the new χ^2 is smaller we accept the new parameter values ($\vec{p}_0 = \vec{p}$), otherwise keeping the original parameter values. We calculate new parameter values and repeat. The parameter values will gradually evolve to the minimum possible χ^2 , by incrementally decreasing the step size one can determine the best fit to some desired accuracy.

2. Checking for convergence to unique minimum.

By repeating this procedure with different starting parameter values in our model space we can determine the uniqueness of this minimum. This is particularly useful in testing the boundaries of the chosen model space. If a minimum is found on a boundary the parameter space must be enlarged. If any 2 parameters are completely correlated, a unique minimum will not be found (*e.g.* l_1 and l'_1)¹⁴ and one must reconsider the allowed parameter space. We will assume from now on that there is only one minimum in our model space and that no two parameters are completely correlated.

3. Determining an appropriate step-size.

To make the MCMC as efficient as possible, one needs to determine an appropriate step size, $\delta\vec{p}$. A simple method of estimating this is by varying individual parameter values away from the minimum, until the difference $\chi^2 - \chi^2_{\min}$ is unity. This choice makes for a good first estimate, and will generally be smaller than or equal to the true parameter errors.

4. Running the chain(s). Enforced constraints.

¹⁴ l'_1 is a LEC associated with a vector-dibaryon-nucleon-nucleon vertex. The LECs l_1 and l'_1 are almost redundant in the np -capture cross section [28].

There are many ways to initiate a MCMC. Some choose to pick an initial point randomly in the model space, while others choose to initiate the chain at the minimum. The latter method avoids the dependence on the prior probability distribution the initial point is generated from and thus reducing the overall convergence length of the chain.

Once the initial point of the chain is chosen, we follow a procedure quite similar to that used in the minimization algorithm. One generates a new set of parameters just as in the minimization algorithm. There is then a set of criteria for accepting or rejecting the new parameter set:

1. if $\Delta\chi^2 = \chi^2(\vec{p}) - \chi^2(\vec{p}_0) < 0$ we accept the new parameter values.
2. otherwise there is a finite probability, $P = \exp(-\Delta\chi^2/2)$ for accepting the point.

For a reasonable step size choice, this allows for the efficient exploration of the “tail” of the parameter likelihood distribution. Whether or not one accepts the new point, a new set of parameters is drawn and this step is repeated until the chain has met its convergence criteria or some maximum length.

5. Checking convergence to a “full” sample.

A relatively simple method to check the convergence of a single chain is to calculate the 1st and 2nd order moments of the chain of a specific length N . We thus calculate the means, variances and covariances of the D parameters:

$$\vec{\mu}(N) = \frac{1}{N} \sum_i^N \vec{p}_i, \quad (26)$$

$$\mathcal{C}(N) = \frac{1}{N-D} \sum_i^N [\vec{p}_i - \vec{\mu}(N)] \otimes [\vec{p}_i - \vec{\mu}(N)], \quad (27)$$

where the variances are the diagonal components of the covariance matrix. As the MCMC converges, these moments of the underlying likelihood distribution will plateau and the fractional difference between the N^{th} and $(N+1)^{\text{th}}$ moments (or functions of the moments, *e.g.* $\det(\mathcal{C})$) should fall like $\sim 1/N$. Thus, we choose N in such a way to reach a certain desired fractional uncertainty.

One can also compare multiple chains and their moments. One can then compare the variance of a single chain to the variance of the chain means, adopting the convergence criteria from [44]. However, since we are starting our chains at the minimum, a single chain is all that is needed once the chain has grown longer than the intrinsic correlation length of the chain (typically \sim few 100’s steps) and the convergence criteria for the single chain is all that is needed.

To meet convergence criteria, chains with length $N \sim 10^6$ are required. The parameter step size is adjusted so that the acceptance is between 25 and 50%. We find that a 40% acceptance rate is most efficient.

References

- [1] P. Descouvemont *et al.*, Atomic Data and Nucl. Data Tables **88** (2004) 203.

best fit values/step-sizes (fm)	minimum χ^2	$\langle\chi^2\rangle \pm \delta\chi^2$	# data
$a_0 \pm \delta a_0 = -23.745 \pm 0.0070$	$\chi_{\text{cap,min}}^2 = 4.63$	5.69 ± 1.48	$N_{\text{cap}} = 6$
$r_0 \pm \delta r_0 = 2.732 \pm 0.0095$	$\chi_{\text{dis,min}}^2 = 4.55$	4.55 ± 0.48	$N_{\text{dis}} = 9$
$\rho_d \pm \delta\rho_d = 1.740 \pm 0.0015$	$\chi_{\text{sct,min}}^2 = 2282.83$	2285.99 ± 2.63	$N_{\text{sct}} = 2124$
$l_1 \pm \delta l_1 = 0.894 \pm 0.0012$	$\chi_{\text{anp,min}}^2 = 10.99$	10.99 ± 0.25	$N_{\text{anp}} = 8$
	$\chi_{\text{tot,min}}^2 = 2303.00$	2308.22 ± 3.22	$N_{\text{tot}} = 2147$

Table 4: This table shows the parameter values at the minimum total χ^2 . The step-sizes should not be confused with error bars. Also evaluated about this point are the step-sizes for each parameter. The second and third columns show the contribution to the minimum and average χ^2 values from each of the types of data (“cap” = capture, “dis” = dissociation, “sct” = scattering, “anp” = analyzing power and “tot” = total χ^2 s, respectively) and the fourth column the number of data points evaluated.

- [2] P. D. Serpico *et al.*, JCAP **0412** (2004) 010.
- [3] R. H. Cyburt, Phys. Rev. D **70** (2004) 023505.
- [4] T. S. Suzuki *et al.*, Astrophys. J. Lett. **439** (1995) L59.
- [5] Y. Nagai *et al.*, Phys. Rev. C **56** (1997) 3173.
- [6] K. Y. Hara *et al.*, Phys. Rev. D **68** (2003) 072001.
- [7] R. Moreh, T. J. Kennett and W. V. Prestwich, Phys. Rev. C **39** (1989) 1247.
- [8] G. R. Bishop *et al.*, Phys. Rev. **80** (1950) 211.
- [9] Y. Nagai, private communication.
- [10] E. C. Schreiber *et al.*, Phys. Rev. C **61** (2000) 061604(R).
- [11] W. Tornow *et al.*, Phys. Lett. **B574** (2003) 8.
- [12] J.-W. Chen and M. J. Savage, Phys. Rev. C **60** (1999) 065205.
- [13] A. S. Johnson and G. M. Hale, Nucl. Phys. **A688** (2001) 566c.
- [14] G. Rupak, Nucl. Phys. **A678** (2000) 405.
- [15] S. Weinberg, hep-th/9702027.
- [16] For recent reviews, see, *e.g.*, D. B. Kaplan, nucl-th/0510023, and references therein.
- [17] P. F. Bedaque and U. van Kolck, Phys. Lett. **B428** (1998) 221; J.-W. Chen, G. Rupak, and M. J. Savage, Nucl. Phys. **A653** (1999) 386 and references therein.

- [18] S. R. Beane *et al.*, in (ed.) M. Shifman, *At the frontier of particle physics*, Vol. 1 133, World Scientific, Singapore (2001); nucl-th/0008064.
- [19] P. F. Bedaque and U. van Kolck, *Ann. Rev. Nucl. Part. Sci.* **52** (2002) 339.
- [20] S. R. Beane, P. F. Bedaque, M. J. Savage, and U. van Kolck, *Nucl. Phys.* **A700** (2002) 377.
- [21] M. Rho, in *AIP Conference Proceedings* (American Institute of Physics, New York, 1999), Vol. 494, p. 391; nucl-th/9908015.
- [22] D. R. Phillips and T. D. Cohen, *Nucl. Phys.* **A668** (2000) 45.
- [23] D. R. Phillips, G. Rupak, and M. J. Savage, *Phys. Lett.* **B473** (2000) 209.
- [24] S. R. Beane and M. J. Savage, *Nucl. Phys.* **A694** (2001) 511.
- [25] S. Ando and K. Kubodera, *Phys. Lett.* **B633** (2006) 253.
- [26] J.-W. Chen, T. Inoue, X. Ji, and Y. Li, nucl-th/0506001.
- [27] S. Beane and M. Savage, *Nucl. Phys.* **A761** (2005) 259.
- [28] S. Ando and C. H. Hyun, *Phys. Rev. C* **72** (2005) 014008.
- [29] S. Nakamura, T. Sato, V. Gudkov, K. Kubodera, *Phys. Rev. C* **63** (2001) 034617; S. Nakamura *et al.*, *Nucl. Phys.* **A707** (2002) 561; S. X. Nakamura, private communication.
- [30] G. M. Hale, private communication; A. S. Johnson and G. M. Hale, *Nucl. Phys.* **A688** (2001) 566c.
- [31] S. Fleming, T. Mehen, and I. W. Stewart, *Nucl. Phys.* **A677** (2000) 313.
- [32] N. Metropolis *et al.*, *J. Chem. Phys.* **21** (1953) 1087.
J. Gubernatis, “The Monte Carlo Method in the Physical Sciences: Celebrating the 50th Anniversary of the Metropolis Algorithm”, *AIP Conference Proceedings*, Volume 690, Melville, NY (2003).
- [33] R. H. Cyburt, B. D. Fields, and K. A. Olive, *New Astronomy* **6** (2001) 215.
- [34] C. Van der Leun and C. Alderliesten, *Nucl. Phys.* **A380** (1982) 261; T. Vyllov, *Sov. J. Nucl. Phys.* **36** (1982) 474; J. Adam, *Czech. J. Phys.* **B33** (1983) 465; G. L. Greene, *Phys. Rev. Lett.* **56** (1986) 819; S. Röttger, *IEEE Trans. Instr. and Meas.* **46** (1997) 560; E. G. Kessler *et al.*, *Phys. Lett.* **A255** (1999) 221.
- [35] NN-OnLine, <http://nn-online.org>.
- [36] A. E. Cox, S. A. R. Wynchank and C. H. Collie, *Nucl. Phys.* **74** (1965) 497.

- [37] D. Cokinos and E. Melkonian, Phys. Rev. C **15** (1977) 1636.
- [38] Callerame *et al.*, Phys. Rev. C **12** (1975) 1423.
- [39] T.-S. Park, D.-P. Min and M. Rho, Phys. Rev. Lett. **74** (1995) 4153; Nucl. Phys. **A596** (1996) 515.
- [40] L. Koester and W. Nistler, Z. Phys. **A272** (1975) 189.
- [41] S. Ando, nucl-th/0509065.
- [42] U. van Kolck, Nucl. Phys. **A752** (2005) 145.
- [43] H. Sadeghi and S. Bayegan, Nucl. Phys. **A753** (2005) 291.
- [44] A. Gelman and D. Rubin, Stat. Science **7** (1992) 457; G. Huey, R.H. Cyburt and B.D. Wandelt, Phys. Rev. D **69** (2004) 103503.